

Impact of Resonant Compton Scattering on Magnetar X-Ray Polarization with QED Vacuum Resonance

TU GUO ^{1,2} AND DONG LAI ^{2,3}

¹*School of Physics and Astronomy, Shanghai Jiao Tong University, Shanghai 200240, China*

²*Tsung-Dao Lee Institute, Shanghai Jiao Tong University, Shanghai, 201210, China*

³*Center for Astrophysics and Planetary Science, Department of Astronomy, Cornell University, Ithaca, NY 14853, USA*

ABSTRACT

Recent observations have revealed significant soft X-ray polarizations from several quiescent magnetars, including the intriguing 90° polarization angle (PA) swing as a function of photon energy for some sources. We present a general semi-analytical framework for calculating energy-dependent soft X-ray polarization signatures from magnetars, consistently incorporating both QED vacuum resonance in the atmosphere and resonant Compton scattering (RCS) in the magnetosphere. Starting from the polarized radiative transfer equation for RCS and treating vacuum-resonance-induced mode conversion as an input, we employ a first-order approximation in RCS optical depth to evaluate the effect of different magnetospheric plasma density (which depends on magnetic twist), drift velocity and temperature, and viewing geometry on the observed radiation. Our analysis reveals that magnetic twist and plasma drift velocity are the critical parameters controlling the impact of RCS on both the absolute polarization degree and its variation across the soft X-ray spectrum. We find that sufficiently strong RCS can wash out the PA swing caused by vacuum resonance. Furthermore, in addition to the QED vacuum resonance effect, significant relativistic signatures arising from plasma drift velocity ($\beta_0 \gtrsim 0.5$) may introduce an extra 90° PA swing in the spectrum. Our calculation framework, based on single-scattering approximation, bypasses the need for complex, multi-dimensional Monte Carlo simulations, providing an analytical pathway for modeling full-surface emission and rotational-phase-resolved radiation from magnetic neutron stars, in support of current and future X-ray polarization missions.

Keywords: Neutron stars (1108), Magnetars (992), Magnetic fields (994), X-ray astronomy (1810), Radiative transfer (1335), Spectropolarimetry (1973)

1. INTRODUCTION

Magnetars are isolated neutron stars endowed with extremely strong magnetic fields (R. C. Duncan & C. Thompson 1992; C. Thompson & R. C. Duncan 1995; C. Kouveliotou et al. 1998; V. M. Kaspi & A. M. Beloborodov 2017). Their surface dipole magnetic fields inferred from spin-down measurements typically reaches $B_{\text{dip}} \sim 10^{14}\text{--}10^{15}$ G. Historically, magnetars' subclasses of Soft Gamma Repeaters (SGRs) and Anomalous X-ray Pulsars (AXPs) were distinguished by their burst behaviors, but both emit persistent soft X-rays (0.5–10 keV) in quiescence with typical luminosities of $L_X \sim 10^{33}\text{--}10^{36}$ erg s⁻¹, much larger than the spindown luminosities. Their quiescent X-ray spectra are commonly described by the combination of a thermal blackbody with

$kT \sim 0.5\text{--}1$ keV, and a non-thermal power law with photon index $\Gamma \sim 2\text{--}4$ (P. M. Woods & C. Thompson 2006). They also emit hard X-rays extending to ~ 100 keV, indicating active corona surrounding magnetars (V. M. Kaspi & A. M. Beloborodov 2017). Despite the rich phenomenology, the integrated X-ray spectrum alone is often inadequate to disentangle the degeneracy among the different emission mechanisms and magnetospheric physics. X-ray polarization measurements can help break this degeneracy and provide constraints on various physical parameters and magnetospheric structure (R. Fernández & S. W. Davis 2011; M. C. Weisskopf et al. 2022; R. Taverna & R. Turolla 2024).

In recent years, the Imaging X-ray Polarimetry Explorer (IXPE) mission (M. C. Weisskopf et al. 2016) has enabled polarimetry measurements in the 2–8 keV band, delivering high-significance detections across multiple sources, including several magnetars. The IXPE

observations of magnetars have revealed two representative types of energy-dependent polarization behavior in soft X-ray band: one class (e.g., 4U 0142+61 in R. Taverna et al. 2022) exhibits a sharp $\sim 90^\circ$ polarization angle (PA) swing at around 5 keV, while the other (e.g., 1RXS J170849.0-400910 in S. Zane et al. 2023) maintains an energy-independent, nearly constant polarization angle.

To explain these spectral polarization features, current theoretical efforts mainly focus on two physical mechanisms: emission from condensed surface (R. Taverna et al. 2022; R. Taverna & R. Turolla 2024), followed by resonant Compton scatterings (RCS) in the magnetosphere (R. Fernández & S. W. Davis 2011; R. Taverna et al. 2014), and the mode conversion effect via vacuum resonance in the atmospheric plasma under strong magnetic fields (D. Lai & W. C. Ho 2002, 2003a; D. Lai 2023; R. M. E. Kelly et al. 2024). Condensed surface requires sufficiently low temperature and high surface binding energy, which is still uncertain (Z. Medin & D. Lai 2006a,b, 2007; A. Y. Potekhin & G. Chabrier 2013). The RCS by charged particles in a twisted magnetosphere can modify the emergent radiation spectrum and polarization profile. This process has been modeled in both semi-analytical 1D frameworks (M. Lyutikov & F. P. Gavriil 2006) and multi-dimensional Monte Carlo simulations with detailed spectral fits (R. Fernández & C. Thompson 2007; L. Nobili et al. 2008a; N. Rea et al. 2008; S. Zane et al. 2009), and further extended to polarization predictions (R. Fernández & S. W. Davis 2011; R. Taverna et al. 2014, 2020; R. Taverna & R. Turolla 2024).

Vacuum resonance, on the other hand, arises from the competition between the plasma-induced birefringence and the vacuum birefringence due to quantum electrodynamics (QED) in strong magnetic fields. When a photon crosses through the resonant layer, it may undergo adiabatic mode conversion, leading to significant change in the polarization (D. Lai & W. C. Ho 2002, 2003a,b). After leaving the atmosphere, the photon may experience significant RCS in the extended magnetosphere or corona, leading to further modifications in polarization.

In this work, we present a general three-dimensional semi-analytical framework that unifies the treatment of vacuum resonance in the atmosphere and RCS in the magnetosphere, with the goal of obtaining the soft X-ray polarization of magnetic neutron stars. To preserve the physical transparency and geometric modularity of our calculation without relying on full Monte Carlo simulations of radiative transport, we use single-scattering approximation. To focus on the key physics, we adopt simplified yet testable idealized assumptions for the po-

larized surface emission that includes the vacuum resonance effect. The structure of this paper is as follows: Section 2 introduces the physical model and computational procedure; Section 3 presents the validation of our fiducial model; Section 4 investigates the X-ray polarization signals for various physical parameters; Section 5 provides the summary and outlook.

2. PHYSICAL FRAMEWORK

To model how resonant Compton scattering (RCS) and QED vacuum resonance jointly shape the X-ray polarization from magnetars, we distinguish the main physical processes with their characteristic locations. This section presents our physical framework for global magnetosphere, the polarized emission and propagation, the RCS formalism, and the computational workflow.

2.1. Global Magnetosphere Model

One of the key characteristics of magnetars is the presence of a highly twisted and dynamically evolving toroidal magnetic field in their magnetosphere (C. Thompson et al. 2002). This arises from the magnetic stress built up in the crust, which induces instabilities, leading to displacement of surface elements and distortion of the magnetic field lines anchored on them. C. Thompson et al. (2002) present a general self-similar, force-free, globally twisted magnetic field model that has been widely used in previous studies (e.g., R. Fernández & C. Thompson 2007; L. Nobili et al. 2008a; R. Fernández & S. W. Davis 2011).

For the purposes of this work, we adopt a simple parametrized model in which a toroidal component proportional to the poloidal field is added, i.e.,

$$\mathbf{B}(\mathbf{r}) = \frac{B_p}{2} \left(\frac{r}{R} \right)^{-3} (2 \cos \theta, \sin \theta, \xi_\tau \sin \theta), \quad (1)$$

where B_p is the surface polar dipole field strength, R is the magnetar radius, and the parameter ξ_τ quantifies the global twist (hence the current distribution). This choice is not strictly force-free, but it captures a quasi-static configuration adequate for our semi-analytic treatment.

We assume a single-charge magnetospheric plasma, with ions being stationary. Given \mathbf{B} , the spatial distribution of current-carrying electrons along the closed field lines is prescribed as (C. Thompson et al. 2002; L. Nobili et al. 2008a; R. Taverna et al. 2020)

$$n_e(\mathbf{r}, \beta_0) = \frac{(\xi_\tau \beta_0^{-1}) B(\mathbf{r})}{4\pi e r}, \quad (2)$$

where $B = |\mathbf{B}(\mathbf{r})|$, $\beta_e \in (-1, 1)$ is the velocity of electrons (normalized by c) along the field lines, and

$\beta_0 = |\langle \beta_e \rangle|$ is the mean drift speed. To determine the full phase-space distribution, we assume a one-dimensional, relativistic, thermal (Maxwell–Jüttner) velocity distribution along the field line, boosted by β_0 (see also L. Nobili et al. 2008a,b):

$$f_1(\beta_e) d\beta_e = \frac{\gamma_0 \gamma_e^3 (1 - \beta_e \beta_0) \exp(-\gamma'/\Theta_e)}{2K_1(1/\Theta_e)} d\beta_e, \quad (3)$$

with $\Theta_e = kT_e/m_e c^2$, $\gamma' = \gamma_e \gamma_0 (1 - \beta_e \beta_0)$, and K_1 the modified Bessel function. This boosting captures the net drift from the magnetic north to south. We assume the magnetospheric temperature T_e is uniform, and treat T_e and β_0 as free parameters. Overall, our magnetosphere model is characterized by three parameters: (ξ_τ, β_0, T_e) .

2.2. Seed Polarized Radiation & Propagation

2.2.1. Surface Emission Model

The bulk of the 2–8 keV photons probed by IXPE originate from the magnetar surface. To model the spectrum and polarization of the surface emission, it is necessary to construct self-consistent magnetic NS atmosphere models that take into account of the QED effect (e.g., W. C. G. Ho & D. Lai 2003; D. Lai & W. C. Ho 2003a; M. van Adelsberg & D. Lai 2006; N. Shalbatas & D. Lai 2012; R. Taverna et al. 2020; I. Caiazzo et al. 2022). Here we summarize the key features of this emission (see also D. Lai 2023).

X-ray photons (with $E = \hbar\omega \ll E_B = \hbar\omega = \hbar eB/m_e c = 1158 B_{14}$ keV) propagating in the magnetized NS atmospheric plasma have two polarization modes: the ordinary mode (O-mode) is mostly polarized parallel to the $\mathbf{k} - \mathbf{B}$ plane, while the extraordinary mode (X-mode) is perpendicular to it, where \mathbf{k} is the photon wave vector and \mathbf{B} is the external magnetic field. The two modes have very different absorption and scattering opacities, with $\kappa_{X\text{-mode}} \sim u_e^{-1} \kappa_{O\text{-mode}}$, where $u_e \equiv (\omega_B/\omega)^2 \gg 1$. Thus, the two modes have very different photosphere densities, with $\rho_{X\text{-mode}} \gg \rho_{O\text{-mode}}$, and the emergent radiation from the NS surface is dominated by the X-mode.

However, the effect of vacuum polarization can change the above picture significantly. In particular, the ‘‘competition’’ between QED-induced vacuum birefringence and plasma-induced birefringence gives rise to a vacuum resonance; for a photon of energy E , this occurs at the density

$$\rho_V \simeq 0.964 Y_e^{-1} B_{14}^2 E_1^2 f^{-2} \text{ g cm}^{-3}, \quad (4)$$

where $Y_e = \langle Z/A \rangle$ is the electron fraction, $E_1 = E/(1 \text{ keV})$, and $f = f(B)$ is a slowly varying function of B and is of order unity.

For $\rho \gtrsim \rho_V$ (where the plasma effect dominates the dielectric tensor) and $\rho \lesssim \rho_V$ (where vacuum polarization dominates), the photon modes (for typical $\theta_{\text{kB}} \neq 0$) are almost linearly polarized, i.e. the linear X-mode and O-mode; at $\rho = \rho_V$, however, the normal modes become circularly polarized. The importance of this vacuum resonance lies in the mode conversion phenomenon (D. Lai & W. C. Ho 2002, 2003a): a X-mode photon emerging from its photosphere (at $\rho_{X\text{-mode}}$) and propagating outwards can convert to the O-mode at ρ_V , provided that its energy satisfies

$$E \gtrsim E_{\text{ad}} = 2.52 (f \tan \theta_{\text{kB}})^{2/3} \left(\frac{1 \text{ cm}}{H_\rho} \right)^{1/3} \text{ keV}, \quad (5)$$

where $H_\rho = |ds/d \ln \rho|$ is the density scale height (evaluated at $\rho = \rho_V$) along the ray. A low-energy ($E \lesssim E_{\text{ad}}$) photon would not experience this conversion. In typical magnetar atmospheres, $\rho_{X\text{-mode}} \gg \rho_V$ is always satisfied. Depending on the relative locations of the O-mode photosphere and vacuum resonance, the X-ray polarization signatures are qualitatively different. Assuming a fully ionized atmosphere (with ion charge Ze and mass Am_p), D. Lai (2023) finds the ratio

$$\rho_V/\rho_{O\text{-mode}} = (B/B_{\text{OV}})^2, \quad (6)$$

with

$$B_{\text{OV}} = 7.8 \times 10^{13} \left(\frac{\mu g_2 \cos \alpha}{Z \mathcal{G} E_1 \sin^2 \theta_{\text{kB}}} \right)^{1/4} \left(\frac{f}{T_6^{1/8}} \right) \text{ G}, \quad (7)$$

where $\mu = A/(1+Z)$ is the ‘‘molecular’’ weight, g_2 is the surface gravity in units of $2 \times 10^{14} \text{ cm/s}^2$, T_6 is surface temperature in units of 10^6 K , and $\mathcal{G} = 1 - \exp(-E/kT)$. For magnetars with surface magnetic fields satisfying $B \lesssim B_{\text{OV}}$, the vacuum resonance lies at a lower density than $\rho_{O\text{-mode}}$, the emergent radiation is dominated by the X-mode for $E \lesssim E_{\text{ad}}$ and by the O-mode for $E \gtrsim E_{\text{ad}}$, i.e., there is a 90° rotation of the polarization angle between $E \lesssim E_{\text{ad}}$ and $E \gtrsim E_{\text{ad}}$. On the other hand, for $B \gtrsim B_{\text{OV}}$, the vacuum resonance lies between $\rho_{O\text{-mode}}$ and $\rho_{X\text{-mode}}$, the emergent radiation from the surface is dominated by X-mode for all E 's.

Quantitative calculations of the atmospheric emission (spectrum and polarization) are fully described in previous works (e.g., W. C. G. Ho & D. Lai 2003; M. van Adelsberg & D. Lai 2006; D. Lai 2023). In this paper, since our focus is on the effect of magnetospheric scatterings, we adopt a simple prescription for the surface emission. For a given spot (located at the polar angles θ_s, ϕ_s) with temperature T_s , the total radiative intensity (in the stellar frame) is given by

$$I_\omega^{(\text{tot})}(\hat{\Omega}) = I_\omega^1(\hat{\Omega}) + I_\omega^2(\hat{\Omega}) \propto \frac{\mu_s^{a-1} \omega^3}{\exp(\hbar\omega/kT_s) - 1}, \quad (8)$$

where μ_s is the (stellar-frame) cosine between the emission direction ($\hat{\Omega}$) and the local magnetic field, and $a \geq 1$ is a beaming parameter (we adopt $a = 1$ for isotropic emission). As discussed above, for $B \lesssim B_{\text{OV}}$, the X-ray polarization degree is set to be either 1 for (i.e., dominated by X-mode) lower energy or -1 (dominated by O-mode) for higher energy by comparing E to E_{ad} , using a smoothed transition (e.g., a Fermi-Dirac function type switch).

2.2.2. General-Relativistic Effects

To describe photon propagation from the NS surface to the scattering region, general-relativistic effects must be considered. For typical magnetar spin periods $P = 2\pi/\Omega = 2\text{--}12$ s, rotational frame-dragging is negligible: $(R\Omega/c)^2 \lesssim 4 \times 10^{-8} R_6^2 P_1^{-2}$ (R. Fernández & S. W. Davis 2011). Thus, the Schwarzschild metric suffices.

Key GR effects include gravitational redshift and light bending. As photons travel to $\gtrsim 10R$ where resonant scattering occurs (see below), the metric at the scattering point is almost flat, with $GM/(10Rc^2) \ll 1$. For redshift, since the photon occupation number $\mathcal{N}(\omega) \propto I_\omega/\omega^3$ is Lorentz invariant, under the redshift $\omega \rightarrow g\omega$ where $g = [1 - 2GM/(Rc^2)]^{1/2}$ the intensity transforms as $I_\omega \rightarrow g^3 I_\omega$. We treat the light bending effect using the mapping between local emission angle α and asymptotic angle ψ as in A. M. Beloborodov (2002), which is accurate for $R \gtrsim 4GM/c^2$.

2.3. Resonant Compton Scattering Formalism

In the outer magnetosphere, photons are scattered by electrons mainly through RCS. For a magnetar with dipole field B_p and twist parameter ξ_τ (see Eq.(1)), RCS occurs at the radius (neglecting the motion of electrons; see below)

$$r_{\text{sc}} = 10.5 R \left(\frac{B_p}{10^{14} \text{ G}} \right)^{1/3} \left(\frac{E}{1 \text{ keV}} \right)^{-1/3} F(\theta), \quad (9)$$

where $F(\theta) = (1 - \frac{3}{4} \sin^2 \theta)^{1/6}$. Given that the Landau level lifetime of gyrating electrons is much shorter than the cyclotron period (R. Fernández & S. W. Davis 2011), electrons can be assumed to remain in the ground state, rendering individual scatterings effectively elastic in the electron rest frame (ERF). We neglect non-resonant scattering and recoil in this work.

2.3.1. Cross Sections

In the Thomson limit, the non-relativistic RCS cross sections were first derived by J. Ventura (1979) (see also Chapter 4 in P. Meszaros 1992). We denote the unit vector along the direction as $\hat{\Omega}$, and the polarization

states as $\alpha \in \{1, 2\} = \{\text{O}, \text{X}\}$. In ERF, the differential cross section takes the form (e.g., L. Nobili et al. 2008a):

$$\left(\frac{d\sigma}{d\Omega} \right)_{\alpha \hat{\Omega}' \rightarrow \beta \hat{\Omega}}^{(\text{ERF})} = \left(\frac{e^2}{m_e c} \right) K'_{\alpha\beta} \delta(\omega - \omega_B), \quad (10)$$

where $\omega = E/\hbar$ is the photon frequency, $\omega_B = eB/m_e c$ is the electron cyclotron frequency, and the coefficients $K_{\alpha\beta}$ are

$$\begin{aligned} K'_{11} &= \frac{3\pi}{8} (\hat{\Omega}' \cdot \hat{B})^2 (\hat{\Omega} \cdot \hat{B})^2, \\ K'_{12} &= \frac{3\pi}{8} (\hat{\Omega}' \cdot \hat{B})^2, \\ K'_{21} &= \frac{3\pi}{8} (\hat{\Omega} \cdot \hat{B})^2, \\ K'_{22} &= \frac{3\pi}{8}. \end{aligned} \quad (11)$$

Note that all the coefficients involving the dot product of unit vectors should be calculated in ERF, so they are all related to the variable β_e . When transforming to the stellar frame, relativistic beaming modifies the differential cross section:

$$\left(\frac{d\sigma}{d\Omega} \right)^{(\text{NS})} = \frac{1}{\gamma_e^2 (1 - \beta_e \mu)^2} \left(\frac{d\sigma}{d\Omega} \right)^{(\text{ERF})}, \quad (12)$$

where $\mu = \hat{\Omega} \cdot \hat{B}$, and the delta function must also transform

$$\delta(\omega - \omega_B)^{(\text{ERF})} \rightarrow \frac{1}{\gamma_e (1 - \beta_e \mu)} \delta(\omega - \omega_D)^{(\text{NS})}, \quad (13)$$

with $\omega_D = \omega_B / [\gamma_e (1 - \beta_e \mu)]$. We denote the differential cross section in the stellar frame as

$$\left(\frac{d\sigma}{d\Omega} \right)_{\alpha \hat{\Omega}' \rightarrow \beta \hat{\Omega}}^{(\text{NS})} = \left(\frac{e^2}{m_e c} \right) K_{\alpha\beta} \delta(\omega - \omega_D) \quad (*)$$

with $K_{\alpha\beta} \equiv K'_{\alpha\beta} / [\gamma_e (1 - \beta_e \mu)]^3$. The scattering radius for photon of frequency ω can be determined by solving the resonance condition $\omega = \omega_D$ for given emission direction and magnetosphere parameters. For the non-relativistic cases with dipole field, solving $\omega = \omega_D \simeq \omega_B$ yields Eq.(9).

In ERF, integrating (10) over scattered directions and summing over β gives the total cross section $\sigma_\alpha(\hat{\Omega}, \beta_e)$ for photons of mode α propagating along $\hat{\Omega}$, which is also Lorentz-invariant:

$$\begin{aligned} \sigma_1 &= \frac{2\pi^2 e^2}{m_e c} (\hat{\Omega} \cdot \hat{B})^2 \delta(\omega - \omega_B), \\ \sigma_2 &= \frac{2\pi^2 e^2}{m_e c} \delta(\omega - \omega_B). \end{aligned} \quad (14)$$

Using the estimate $\sigma \simeq (\pi^2 e^2 / m_e c) \delta(\omega - \omega_B)$ and Eq.(2) for n_e , we obtain the characteristic optical depth across the resonant layer (see also C. Thompson et al. 2002):

$$\tau_0(\hat{\Omega}) \equiv \int ds n_e \sigma = \frac{\pi \xi_\tau}{4\beta_0} \frac{B}{r_{sc}} \left| \frac{dB}{ds} \right|^{-1} \sim \frac{\pi \xi_\tau}{4\beta_0}, \quad (15)$$

where ds is integrated across the RCS layer along $\hat{\Omega}$ and $|\frac{dB}{ds}| = (\hat{\Omega} \cdot \nabla)B \sim B/r_{sc}$ is the directional derivative of B along the photon path. We note that the optical depth is independent of energy. For specific polarization mode α , we can obtain the corresponding optical depth for specific polarization mode $\tau_\alpha(\hat{\Omega}) \equiv \int ds d\beta_e n_e f_1(\beta_e) \sigma_\alpha$. Note that the estimated $\tau_\alpha \sim 1$ indicates that each emergent photon is expected to be scattered once on average in the magnetosphere.

2.3.2. Polarized Radiative Transfer in magnetosphere

After a photon leaves the NS surface, it propagates in the magnetosphere, whose dielectric property is dominated by vacuum polarization (J. S. Heyl et al. 2003). At small radii, the photon's polarization state evolves adiabatically following the varying magnetic field it experiences, such that the specific mode intensity is constant (except for the GR corrections discussed in section 2.2.2)⁴.

Near the RCS layer, the transfer equation for polarized intensity $I_\omega^\alpha(\hat{\Omega}) \equiv I_\omega^\alpha(\hat{\Omega}, \mathbf{r}_{sc})$ (where the \mathbf{r}_{sc} dependence highlights the dependence on the scattering location) of mode α and frequency ω is given by (in the NS frame)

$$\begin{aligned} (\hat{\Omega} \cdot \nabla) I_\omega^\alpha(\hat{\Omega}) &= - \int d\beta_e n_e f_1(\beta_e) \sigma_\alpha(\hat{\Omega}, \beta_e) I_\omega^\alpha(\hat{\Omega}) \\ &+ \sum_\beta \int d\beta_e \oint d\Omega' n_e f_1(\beta_e) \eta^{-3} I_{\eta\omega}^\beta(\hat{\Omega}') \left(\frac{d\sigma}{d\Omega'} \right)_{\beta\hat{\Omega}' \rightarrow \alpha\hat{\Omega}}^{(NS)}, \end{aligned} \quad (16)$$

where $\eta = \eta(\beta_e, \hat{\mathbf{B}}, \hat{\Omega}', \hat{\Omega}) = (1 - \beta_e^2) / [(1 - \beta_e \cos \theta_1)(1 + \beta_e \cos \theta_2)]$ is the Doppler-shift factor linking the incident ($\eta\omega$) and scattered (ω) frequencies, $\cos \theta_1 = \hat{\Omega}' \cdot \hat{\mathbf{B}}$, and $\cos \theta_2 = \hat{\Omega} \cdot \hat{\mathbf{B}}$ are calculated in the NS frame and ERF respectively, and the η^{-3} factor represents the intensity rescaling through scattering (i.e. Comptonization). We denote the position vector of a small emission patch on the NS surface as $R\hat{\Omega}_s$, the position vector for scattering location as $\mathbf{r}_{sc} = r_{sc}\hat{\Omega}_0$.

⁴ An exception occurs when the photon encounters the quasi-tangential (QT) point, where the photon momentum is nearly aligned with the local magnetic field. The X-ray polarization may change significantly when the photon passes through the QT region (C. Wang & D. Lai 2009). Since only a small fraction of the NS surface radiation is affected by the quasi-tangential propagation, we shall neglect this effect in this paper.

Then the incoming direction vector can be calculated as $\hat{\Omega}' = (r_{sc}\hat{\Omega}_0 - R\hat{\Omega}_s) / |r_{sc}\hat{\Omega}_0 - R\hat{\Omega}_s|$. The first term in the RHS of Eq.(16) represents the attenuation of the incoming intensity along $\hat{\Omega}$, and the second term represents the scattered-in contributions. For non-relativistic electrons ($\beta_e \ll 1$), given the narrowness of the resonance, the scattering occurs on a thin surface. For single scatterings, Eq.(16) can be solved to yield the relationship between the incoming (before RCS) intensity $I_{\omega,in}^\alpha$ and the outgoing (after RCS) intensity $I_{\omega,out}^\alpha$ as

$$I_{\omega,out}^\alpha(\hat{\Omega}) = I_{\omega,out}^{\alpha(I)}(\hat{\Omega}) + I_{\omega,out}^{\alpha(II)}(\hat{\Omega}). \quad (17)$$

The first term is the attenuated incoming intensity that propagates along $\hat{\Omega}$:

$$I_{\omega,out}^{\alpha(I)}(\hat{\Omega}) = I_{\omega,in}^\alpha(\hat{\Omega}) \exp(-\tau_\alpha), \quad (18)$$

where $\tau_\alpha(\hat{\Omega}) = \int ds d\beta_e n_e f_1(\beta_e) \sigma_\alpha$. The second term in Eq. (17) represents the scattered-in part, which is given by

$$\begin{aligned} I_{\omega,out}^{\alpha(II)}(\hat{\Omega}) &= \sum_\beta \int ds d\beta_e \oint d\Omega' n_e f_1(\beta_e) \\ &\times \eta^{-3} I_{\eta\omega,in}^\beta(\hat{\Omega}') \left(\frac{d\sigma}{d\Omega'} \right)_{\beta\hat{\Omega}' \rightarrow \alpha\hat{\Omega}}^{(NS)}. \end{aligned} \quad (19)$$

In Eq.(19), the integration over ds can be simplified using the delta function in the cross section, and the integration over $d\Omega'$ for a given scattering site \mathbf{r}_{sc} can be written as

$$\oint d\Omega' = \oint \frac{d\mathbf{A}_s \cdot \hat{\Omega}'}{|\mathbf{r}_{sc} - R\hat{\Omega}_s|^2} = \int \frac{dA_s (\hat{\Omega}_s \cdot \hat{\Omega}')}{|\mathbf{r}_{sc} - R\hat{\Omega}_s|^2} \Theta(\hat{\Omega}_s \cdot \hat{\Omega}'), \quad (20)$$

where $d\mathbf{A}_s = \hat{\Omega}_s dA_s$ is the surface element vector of the emission spot on NS surface (see figure 1). Note that we have included a Heaviside function $\Theta(\hat{\Omega}_s \cdot \hat{\Omega}')$ to ensure that only photons emitted outward from the surface are accounted for. Substituting the expression of n_e and $(d\sigma/d\Omega')$ with the simplifications above, Eq.(19) can be rewritten as

$$\begin{aligned} I_{\omega,out}^{\alpha(II)}(\hat{\Omega}) &= \int \frac{dA_s (\hat{\Omega}_s \cdot \hat{\Omega}') \Theta(\hat{\Omega}_s \cdot \hat{\Omega}')}{4\pi |\mathbf{r}_{sc} - R\hat{\Omega}_s|^2} \frac{\xi_\tau}{\beta_0} \sum_\beta \int d\beta_e f_1(\beta_e) \\ &\times \eta^{-3} I_{\eta\omega,in}^\beta(\hat{\Omega}') K_{\beta\alpha}(\hat{\Omega}' \rightarrow \hat{\Omega}) \frac{B}{r_{sc}} \left| \frac{\partial}{\partial s} \left[\frac{B}{\gamma_e(1 - \beta_e \mu)} \right] \right|^{-1}, \end{aligned} \quad (21)$$

Where $K_{\beta\alpha}(\hat{\Omega}' \rightarrow \hat{\Omega})$ is given by Eq.(*). Eqs.(17), (18) and (21) give the total outgoing intensity after one scattering. We expect that the single-scattering approximation is valid when $\tau_\alpha \lesssim 1$. We may still apply it for the

$\tau_\alpha \gtrsim 1$ cases to show qualitative physical trend. Higher-order solutions can be obtained perturbatively, analogous to that in M. Lyutikov & F. P. Gavril (2006), where an analytical solution for the one-dimensional case is given.

After RCS, an outgoing photon continues to propagate in the magnetosphere, with its polarization state evolving adiabatically, i.e., $I_\omega^\alpha(\hat{\Omega}) = \text{constant}$. Eventually, the photon reaches the ‘‘polarization-limiting radius’’ r_{pl} , beyond which the polarization state is frozen. The value of r_{pl} depends on the photon energy E , the dipole field strength B_p and the magnetar rotation rate, and generally $r_{\text{pl}}/R \gtrsim 100$ (M. van Adelsberg & D. Lai 2006). Since $r_{\text{pl}} \gg r_{\text{sc}}$, regardless of the structure and shape of the RCS layer, the radiation emerging from the layer with mode intensities I_ω^α evolves adiabatically in the magnetosphere such that the radiation at $r > r_{\text{pl}}$ consists of approximately the same X-mode and O-mode intensities as those emerging from the RCS layer, with a small mixture of circular polarization generated around r_{pl} . See D. Lai (2023) for more details.

2.4. Computational Workflow

In our magnetar radiation model, different physical processes are separated cleanly by their characteristic radial scales: emission near the surface, propagation and scattering through the magnetosphere, and polarization evolution from the scattering layer to the polarization limiting radius. Our calculations are divided into three steps:

1. *Emission near the surface under vacuum resonance*: Near the neutron star surface and atmosphere, the dominant process is polarized X-ray emission influenced by QED vacuum resonance. This region has been extensively studied (e.g., M. van Adelsberg & D. Lai 2006; D. Lai 2023; R. M. E. Kelly et al. 2024), allowing us to directly adopt previously computed emissivity profiles as input. In this work, we use a simplified prescription for the surface emission, as described in section 2.2.1.
2. *Adiabatic propagation from surface and RCS*: As discussed, resonant scattering occurs at $\sim 10R$. After emission from the NS surface, the photon polarization evolves adiabatically following the magnetic field and propagates solely under gravitational effects until scattering. Light bending is handled using the method of A. M. Beloborodov (2002). Specifically, the light-bending mapping between local emission angle α and asymptotic angle ψ corresponds to a mapping between $(\hat{\Omega}_s \cdot \hat{\Omega}')$ at RCS layer and that at the NS surface, which

is used in Eq.(21). Note that the dot product in Eq.(21) represents the cosine of the asymptotic angle after light bending. We shall see later that this mapping is also applied in calculating the flux contribution of $I_{\omega,\text{out}}^{\alpha(I)}$, where a similar dot product is also presented.

3. *Continuing adiabatic propagation to large distances where polarization freezes*: After scattering, the polarization continues to evolve adiabatically until the photon reaches the polarization limiting radius ($\gg r_{\text{sc}}$), where the polarization freezes and aligns coherently, yielding the observable net polarization. The observed flux is computed by integrating the contributions from all locations on the scattering surface. Specifically, we integrate the mode-resolved intensity $I_{\text{out},\omega}^\alpha(\hat{\Omega}, \mathbf{r}_{\text{sc}}(\hat{\Omega}_0))$ over the outer surface of the scattering layer.

Figure 1 illustrates the geometric framework for our calculations of the magnetar X-ray radiation. Panel (a) defines the geometry: we set up a Cartesian coordinate system with the magnetic axis along the z -axis, and the observer’s line of sight (LOS) is in the yz plane at angle θ from z axis. The radiation source (position vector $R\hat{\Omega}_s$) is located at (θ_s, ϕ_s) on the NS surface. The location on the scattering surface is denoted by $\mathbf{r}_{\text{sc}} = r_{\text{sc}}\hat{\Omega}_0$. The direction of the incoming photon is $\hat{\Omega}'$, and that of the scattered photon is $\hat{\Omega}$. Two photon populations contribute to the observed flux, as discussed in Section 2.3.2 and illustrated in Figure 1:

- *Attenuation term* $I_{\omega,\text{out}}^{\alpha(I)}(\hat{\Omega})$ — photons emitted directly toward the observer, attenuated by scattering;
- *Scattered-in term* $I_{\omega,\text{out}}^{\alpha(\text{II})}(\hat{\Omega})$ — photons from all other directions scattered into the LOS.

Panel (b) of Figure 1 shows how scattered rays reach the observer. Ignoring stellar surface occultation, the total polarized flux in mode α is given by

$$\mathcal{F}_\omega^\alpha = \mathcal{F}_\omega^{\alpha(I)} + \mathcal{F}_\omega^{\alpha(\text{II})} = \int I_{\omega,\text{out}}^\alpha(\hat{\Omega}) (\hat{\Omega} \cdot \hat{\Omega}_{\text{obs}}) d\Omega. \quad (22)$$

Since the rays reaching the observer from different locations on the scattering surface are nearly parallel, we have $(\hat{\Omega} \cdot \hat{\Omega}_{\text{obs}}) = 1$. Substituting Eqs.(17), (18) and (21) into Eq.(22), using $d\Omega = |d\mathbf{A} \cdot \hat{\Omega}_{\text{obs}}|/D^2$ with $d\mathbf{A}$ being the area element vector of the scattering surface

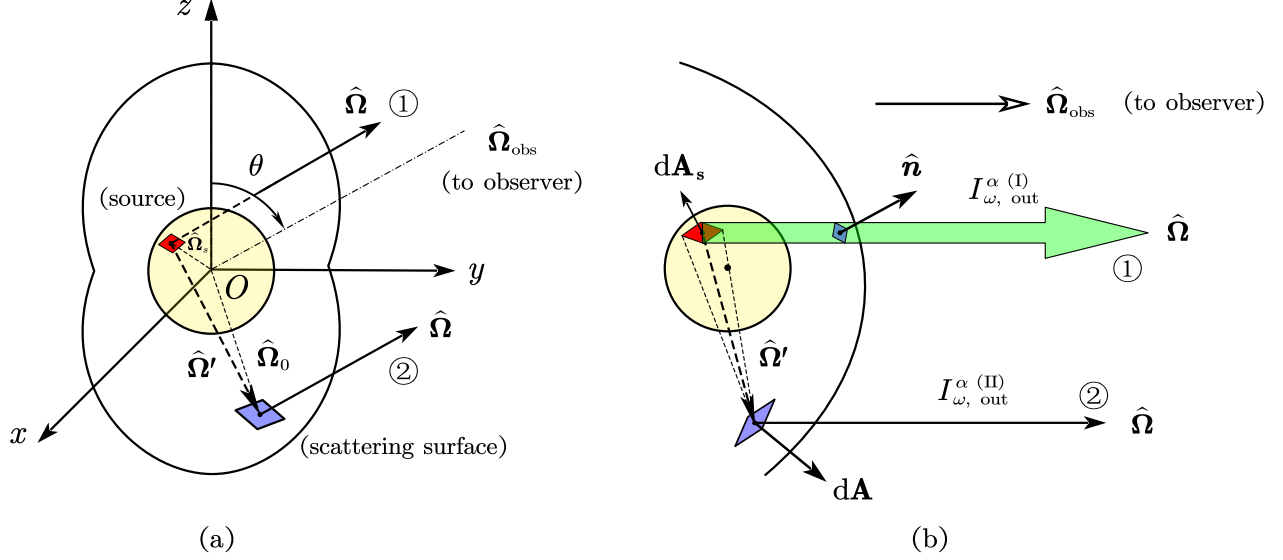


Figure 1. Schematic picture of the radiative transfer with resonant Compton scattering and the computation of the observed polarization flux. The surface element of the NS is $d\mathbf{A}_s = \hat{\Omega}_s dA_s$. The scattering surface element (located at $\mathbf{r}_{sc} = r_{sc}\hat{\Omega}_{sc}$) is denoted by $d\mathbf{A}$. The scattered radiation propagates along the direction $\hat{\Omega} \simeq \hat{\Omega}_{obs}$, and the incident radiation (before scattering) propagates along $\hat{\Omega}' = (r_{sc}\hat{\Omega}_0 - R\hat{\Omega}_s)/|r_{sc}\hat{\Omega}_0 - R\hat{\Omega}_s|$. The magnetic axis of the magnetar is along the z -axis, and $\hat{\Omega}_{obs}$ is in the yz plane, with the angle between $\hat{\Omega}_{obs}$ and z -axis being θ .

and D being the distance to the observer, we obtain

$$\begin{aligned} \mathcal{F}_\omega^{\alpha (I)} &= \frac{A_s}{D^2} (\hat{\Omega}_s \cdot \hat{\Omega}_{obs}) I_{\omega, in}^\alpha(\hat{\Omega}_{obs}) \exp(-\tau_\alpha), \\ \mathcal{F}_\omega^{\alpha (II)} &= \frac{A_s}{4\pi D^2} \frac{\xi_\tau}{\beta_0} \sum_\beta \int d\beta_e \oint d\Omega_0 f_1(\beta_e) \eta^{-3} I_{\eta\omega, in}^\beta(\hat{\Omega}') \\ &\quad \times \frac{r_{sc}^2 |\hat{\mathbf{n}} \cdot \hat{\Omega}_{obs}|}{|r_{sc} - R\hat{\Omega}_s|^2} (\hat{\Omega}_s \cdot \hat{\Omega}') \Theta(\hat{\Omega}_s \cdot \hat{\Omega}') \\ &\quad \times K_{\beta\alpha}(\hat{\Omega}' \rightarrow \hat{\Omega}_{obs}) \frac{B}{r_{sc}} \left| \frac{\partial}{\partial s} \left[\frac{B}{\gamma_e(1 - \beta_e\mu)} \right] \right|^{-1}, \end{aligned} \quad (23)$$

where we have assumed a small emission surface area A_s on the NS surface — in general, an integration over the whole surface can be performed. In Eq.(23), we have used that $d\mathbf{A} = \hat{\mathbf{n}} r_{sc}^2 d\Omega_0$ with $\hat{\mathbf{n}}$ being the surface normal vector of the scattering surface. Note that the final form of the first expression in Eq.(23) does not involve integration over the scattering surface, since only photons emitted directly toward the observer without scattering contribute to this term. Also note that to simplify notations, the dot products $(\hat{\Omega}_s \cdot \hat{\Omega}_{obs})$ and $(\hat{\Omega}_s \cdot \hat{\Omega}')$ in Eq.(23) do not include GR effect. As mentioned before, when substituting the incoming intensity $I_{\omega, in}^\alpha$, we must account for GR light bending from the NS surface to the scattering layer. In this context, the dot products $(\hat{\Omega}_s \cdot \hat{\Omega}_{obs})$ and $(\hat{\Omega}_s \cdot \hat{\Omega}')$ represent the effective

projection of the emission area onto the incoming direction $\hat{\Omega}'$ after light bending. Similarly, by re-mapping the $(\hat{\Omega}_s \cdot \hat{\Omega}_{obs})$ back to the NS surface using the method of [A. M. Beloborodov \(2002\)](#), we can incorporate the GR effect in Eq.(23).

After we obtain the fluxes $\mathcal{F}_\omega^\alpha$ of each mode, the linear polarization degree can be calculated as

$$P_L(\omega) = \frac{\mathcal{F}_\omega^2 - \mathcal{F}_\omega^1}{\mathcal{F}_\omega^2 + \mathcal{F}_\omega^1}. \quad (24)$$

3. RESULT OF SIMPLIFIED FIDUCIAL MODEL

To identify how each ingredient in our semi-analytic treatment shapes the observables, we begin with a simplified model for preliminary analysis. Throughout this section, we adopt a pure dipole field with a cold-plasma approximation, ignoring relativistic effects. The electron number density follows Eq.(2), with the parameter $\zeta \equiv \xi_\tau/\beta_0$ controlling the electron density (see Eq.(2)) and hence the effective RCS strength (see Eq.(15)), independently of the field geometry. Under these assumptions, the mode-resolved optical depths can be calculated as $\tau_\alpha^{(NR)} = \int ds n_e \sigma_\alpha^{(NR)}$ and the flux can be sim-

plified to

$$\begin{aligned} \mathcal{F}_\omega^{\alpha(\text{NR,I})} &= \frac{A_s \widehat{\Omega}_s \cdot \widehat{\Omega}_{\text{obs}}}{D^2} I_{\omega,\text{in}}^\alpha(\widehat{\Omega}_{\text{obs}}) \exp\left(-\tau_\alpha^{\text{(NR)}}\right), \\ \mathcal{F}_\omega^{\alpha(\text{NR,II})} &= \frac{A_s \zeta}{4\pi D^2} \sum_\beta \oint d\Omega_0 K_{\beta\alpha} I_{\omega,\text{in}}^\beta(\widehat{\Omega}') \frac{B}{r_{\text{sc}}} \left| \frac{dB}{ds} \right|^{-1} \\ &\quad \times \frac{r_{\text{sc}}^2 \left| \widehat{\mathbf{n}} \cdot \widehat{\Omega}_{\text{obs}} \right|}{\left| r_{\text{sc}} - R\widehat{\Omega}_s \right|^2} \left(\widehat{\Omega}_s \cdot \widehat{\Omega}' \right) \Theta \left(\widehat{\Omega}_s \cdot \widehat{\Omega}' \right). \end{aligned} \quad (25)$$

For our fiducial setup, we adopt magnetar parameters $B_p = 10^{14}$ G, $R = 10$ km, and $kT_s = 0.6$ keV, with the emission point located at $(\theta_s, \phi_s) = (65^\circ, 30^\circ)$, and the observer's viewing angle set to $\theta = 25^\circ$. We compute the polarized fluxes and linear polarization degree in the IXPE band (2–8 keV).

Figure 2 illustrates the impact of varying ζ on both the mode-resolved spectra and polarization of the observed radiation. For weaker scatterings with small ζ (where the single-scattering approximation is valid), the initially dominant mode is attenuated, while the subdominant mode gains through scatterings, reducing the O/X and spectral contrast. For stronger scatterings with larger ζ , the total flux increases, since the scattered-in term scales directly with electron density. As the density becomes too high, our single-scattering approximation may overestimate the flux. In this regime, the spectral shapes of the O- and X-modes become similar.

The right panel of Figure 2 shows the corresponding linear polarization degree $P_L(\omega)$ as a function of the photon energy. As RCS strength increases, P_L flattens, and it becomes positive for all photon energies in the case of $\zeta = 7$. Thus, the original mode-switching signature may disappear in the strong scattering cases. This phenomenon will be discussed in more detail in Sections 4 and 5.

Regarding the validity of our calculations, all the results above rely on the assumption of single-scattering, i.e., a small resonant optical depth. Our numerical checks confirm that the estimated optical depth ($\sim 0.1 - 1$) from Section 2 is valid. Specifically, for the geometry used above, we find $\tau \lesssim 1$ when $\zeta \lesssim 3.7$, supporting the accuracy of the single-scattering solution in this range. Notably, the disappearance of mode switch in our calculations occurs at $\zeta \gtrsim 5.6$, where the single-scattering approximation becomes questionable.

4. FULL MODEL: PARAMETER STUDY

In this section, we adopt the full model setup, including both the thermal velocity distribution of magnetospheric electrons and the special & general relativistic effects. When the electron velocities are thermal about

a mean drift, the resonance condition $\omega = \omega_D(\mathbf{r}, \mu, \beta_e)$ no longer selects a single geometric surface but broadens into a thin region centered around the drift-defined resonant surface, with thickness set by the velocity distribution.

To include the GR effects, we fix the compactness of the NS at

$$u \equiv \frac{2GM}{Rc^2} = 0.3, \quad (26)$$

and the other NS parameters are held consistent with the previous section. Since all photons experience nearly the same redshift from emission to scattering in our geometries, GR mainly introduces a common rescaling in the intensity and energy. Therefore, we interpret the surface temperature kT_s as the effective blackbody temperature of X-ray emission just before scattering, the same as in Section 3.

Under the current model, the scattering is controlled by the parameter set:

$$\{\xi_\tau, \beta_0, kT_e, kT_s, \theta, M\}. \quad (27)$$

In the survey below, we fix kT_s , E_{ad} and M , and vary $(\xi_\tau, \beta_0, kT_e, \theta)$, while all other parameters are the same as in Section 3.

4.1. Optical-depth Dependence

Before analyzing the spectra and polarization, it is useful to delineate under what conditions the single-scattering solution is valid. The resonant optical depth τ_α (for mode α) is primarily controlled by (ξ_τ, β_0) , which set the electron density and beaming.

Figure 3 presents the heatmap of the characteristic optical depth τ_0 (see Eq.(15)), calculated at $kT_e = 10$ keV and $\theta = 35^\circ$, as functions of ξ_τ and β_0 . The $\tau_0 = 1$ contour marks the single-scattering boundary; the $\tau_0 = 0.4$ contour corresponds to $\lesssim 10\%$ error for a first-order expansion of $\exp(-\tau)$. As expected, larger ξ_τ and smaller β_0 yield higher τ_α due to the increased particle density.

Using the twist parametrization defined in Eq.(1), the total pole-to-pole twist angle is approximately

$$\Delta\phi = \int_0^\pi \frac{B_\phi}{B_\theta \sin\theta} d\theta \sim \pi\xi_\tau, \quad (28)$$

so the ranges adopted in previous Monte Carlo studies (e.g., [L. Nobili et al. 2008a](#), [R. Fernández & S. W. Davis 2011](#)) fall largely within the $\tau_0 \lesssim 1$ regime in Figure 3.

4.2. Spectra and Polarization

We survey on four key parameters: the viewing angle θ , the magnetic twist ξ_τ , the mean drift speed of electrons β_0 , and the plasma temperature kT_e . The

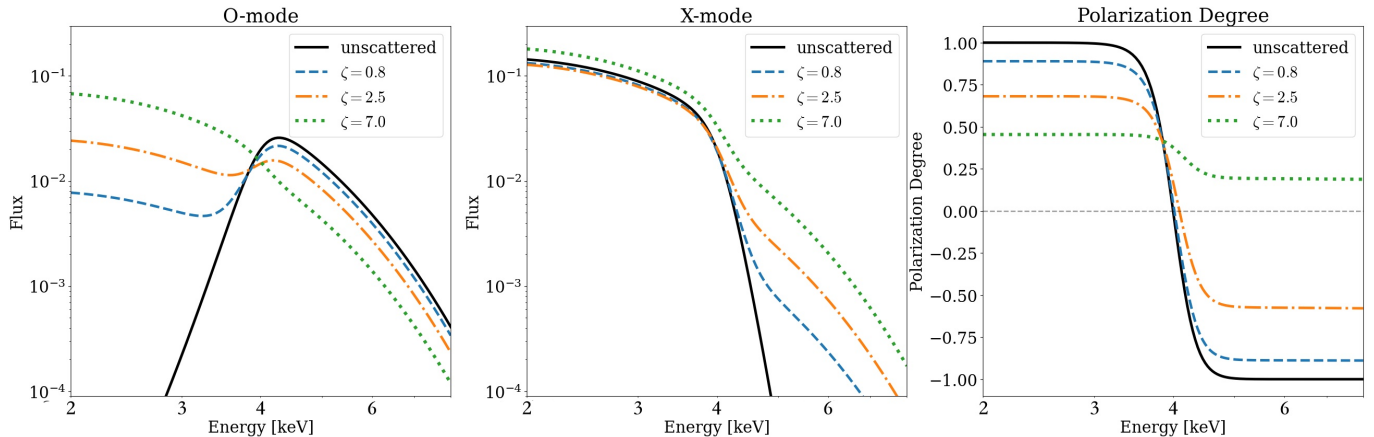


Figure 2. Flux and polarization spectra for different scattering strengths compared to the unscattered case in the simplified setup with $B_p = 10^{14}$ G, $kT = 0.6$ keV, $R = 10$ km, a hot spot at $(\theta_s, \phi_s) = (65^\circ, 30^\circ)$, viewing angle $\theta = 25^\circ$, and varying $\zeta \equiv \xi_\tau/\beta_0 = 0.8, 2.5, 7.0$ (see Eqs.(2) and (15)). *Left and middle:* the relative O-mode and X-mode fluxes. *Right:* the corresponding linear polarization degree $P_L(\omega)$ as a function of energy.

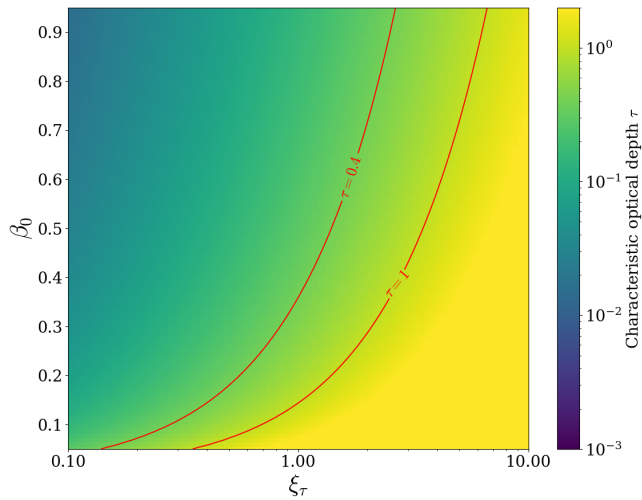


Figure 3. Heatmap of the characteristic resonant optical depth in the full model. The parameters are: $B_p = 10^{14}$ G, $R = 10$ km, $kT_e = 10$ keV, $kT_s = 0.6$ keV, a hot spot at $(\theta_s, \phi_s) = (53^\circ, 37^\circ)$, viewing angle $\theta = 35^\circ$. Contours for $\tau_\alpha = 1$ and $\tau_\alpha = 0.4$ delineate the validity of single-scattering/first-order approximation regime.

observed flux is computed as a multidimensional integral over the emission direction, scattering geometry, and electron velocity. Given the smoothness of the integration kernel, we evaluate the integral via Monte Carlo quadrature with 10^6 samples per configuration. This choice introduces small statistical fluctuations, or “noise”, in the results, but enables significantly improved computational speed and numerical stability, resulting in a relative numerical uncertainty below 0.5%.

Viewing geometry.—Figure 4 presents the flux and polarization spectra for various viewing angles. For this plot, we consider a single hot spot located at the equa-

tor $(\theta_s, \phi_s) = (90^\circ, 37^\circ)$ to highlight the north–south asymmetries (see L. Nobili et al. 2008a). Notably, pairs of LOS angles symmetric about the equator (e.g., 37° and 143°) yield markedly different flux and polarization spectra, demonstrating the impact of Doppler shifts caused by large-scale net currents flowing from magnetic north to south. Importantly, the polarization curves retain the qualitative behavior previously seen in Section 3: RCS may suppress or erase the intrinsic mode-conversion feature that would otherwise appear in the emission. For instance, the curve corresponding to $\theta = 37^\circ$ shows sign flips in polarization degree, whereas for other angles P_L remains positive across the energy band. We verify that in this parameter setting, the optical depth $\tau_\alpha(\theta)$ remains well below unity (typically $\lesssim 0.1$), indicating that even single scatterings can significantly modify the polarization signature, despite the overall low scattering probability.

Magnetic twist.—Figure 5 explores how varying the magnetic twist ξ_τ affects the resulting flux and polarization spectra. The twist primarily modulates the plasma density and hence the scattering strength. As ξ_τ increases, the flux spectra show progressively larger deviations from the unscattered case, exhibiting the “spectral smoothing” noted in Section 3. However, relativistic effects become more prominent in the polarization spectra, especially at higher photon energies. Compared to the non-relativistic case, special-relativistic effects cause the polarization degree to rise again at higher energies. In some cases, the polarization curve crosses zero twice within the IXPE band, indicating the possibility for multiple 90° PA swings (this is also seen in pure QED scenario, see D. Lai 2023 and R. M. E. Kelly et al. 2024).

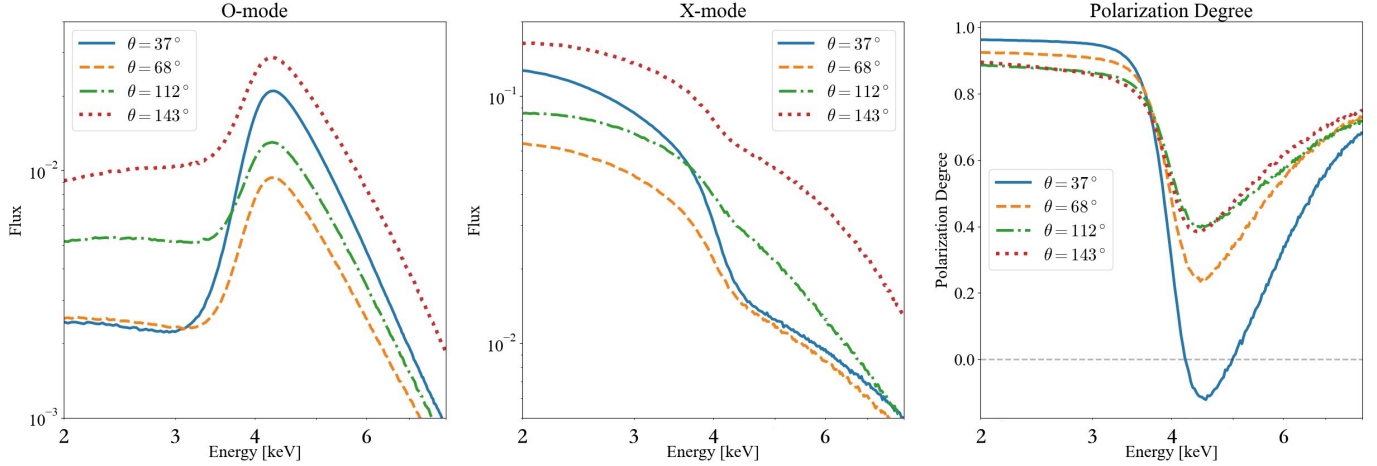


Figure 4. Flux and polarization spectra for different observer viewing angles in the full model. The parameters are: $B_p = 10^{14}$ G, $R = 10$ km, $kT_e = 10$ keV, $kT_s = 0.6$ keV, $\xi_\tau = 0.2$, $\beta_0 = 0.5$, and a hot spot at $(\theta_s, \phi_s) = (90^\circ, 37^\circ)$. Results are shown for the viewing angle $\theta = 37^\circ, 68^\circ, 112^\circ, 143^\circ$.

For sufficiently large ξ_τ , polarization remains strictly positive, and mode switching disappears.

Electron drift velocity.—Figure 6 shows the impact of changing the average drift velocity β_0 on the flux and polarization spectra. Like ξ_τ , the parameter β_0 influences both the plasma density and the strength of SR beaming. While its effects on the flux spectrum resemble those of increasing ξ_τ , the behavior of the polarization curves offers further diagnostic insight. Decreasing β_0 increases the particle density and weakens SR beaming, suppressing P_L at low energies and flattening its high-energy tail that was initially raised by SR; this is consistent with the non-relativistic trend discussed in Section 3. However, in terms of the first zero-crossing energy—the location where initial 90° PA swing occurs—the effect of varying β_0 is subtler than that of ξ_τ . The transition slopes remain similar, indicating that β_0 mainly sets the vertical offset (baseline) of P_L , while it plays a secondary role in slope that shapes the crossing location.⁵

Together, these two main control parameters— ξ_τ and β_0 —determine how RCS reshapes polarization spectra. Two principal effects emerge: (i) a reduction in both the absolute value and spectral variation of the polarization degree; and (ii) a high-energy rise of P_L driven by SR mode redistribution. Even in the single-scattering regime, RCS may erase the mode switch feature that is originally present in the emission. To understand this

trend, consider the polarized RCS cross sections in ERF (see Eq.(10)):

$$\begin{aligned}\sigma_{1-1} &= \frac{1}{3}\sigma_{1-2} = \frac{\pi^2 e^2}{2m_e c} \delta(\omega - \omega_B) \left(\boldsymbol{\Omega}' \cdot \hat{\mathbf{B}} \right)^2, \\ \sigma_{2-2} &= 3\sigma_{2-1} = \frac{3\pi^2 e^2}{2m_e c} \delta(\omega - \omega_B).\end{aligned}\quad (29)$$

These expressions represent the relative probabilities for photons to scatter between specific initial and final polarization states. Notably, regardless of the initial state, scattering tends to populate the X-mode (the polarization index $\alpha = 2$) more efficiently. Since the original emission is X-dominated at low energies, RCS has limited effect there, whereas at higher energies (O-dominated) RCS transfers power to X, producing the characteristic high-energy rise of P_L . The electron density mainly rescales P_L , while the SR effects modulate its slope, particularly in the high-energy tail. Together, they reshape the polarization distribution and influence the energy at which mode switches occurs.

Thermal broadening.—Finally, Figure 7 examines the role of plasma temperature kT_e in shaping the flux and polarization spectra. For visibility, the flux panels are vertically rescaled. Compared to the single-velocity case, thermal motion only induces modest changes. Unlike β_0 , which parameterizes the bulk drift, increasing kT_e only broadens the velocity distribution around β_0 . This tends to average out the variation in Doppler effects over electron speeds, resulting in a behavior that closely resembles the single-velocity case at the same β_0 . This is consistent with previous findings by L. Nobili et al. (2008a).

⁵ A dynamic analogy may be helpful: imagine the polarization curve as a catenary suspended between a high left platform and a vertical wall on the right. Increasing relativistic effect raises the right anchor, steepening the tail of the curve while leaving its middle largely unchanged.

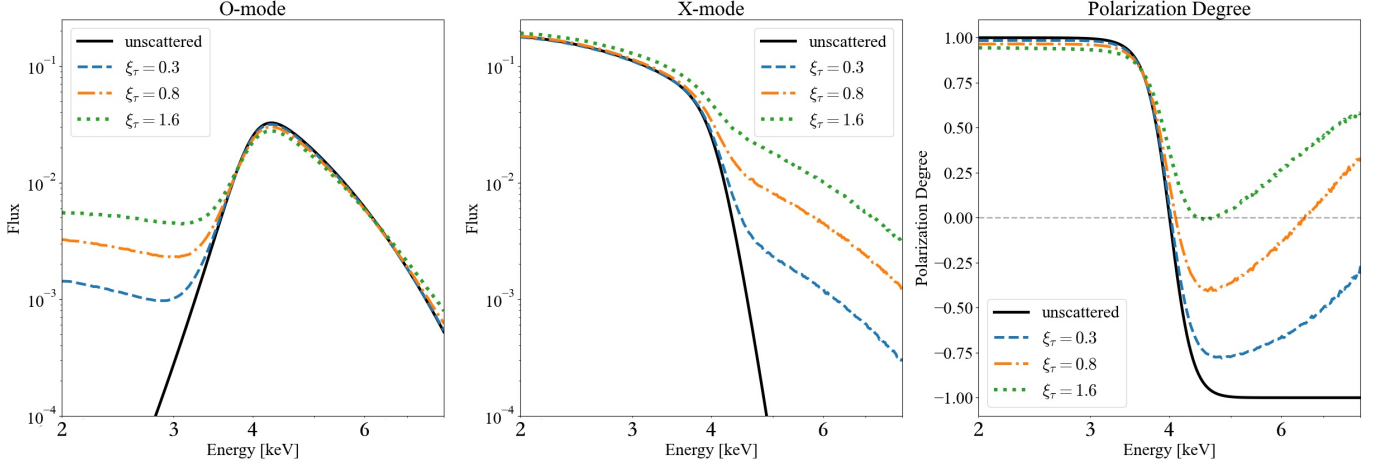


Figure 5. Flux and polarization spectra for different magnetospheric twist parameters in the full model. The parameters are: $B_p = 10^{14}$ G, $R = 10$ km, $kT_e = 10$ keV, $kT_s = 0.6$ keV, $\theta = 35^\circ$, $\beta_0 = 0.5$, and a hot spot at $(\theta_s, \phi_s) = (53^\circ, 37^\circ)$. Results are shown for magnetic twist $\xi_r = 0.3, 0.8, 1.6$, and are compared with the unscattered case.

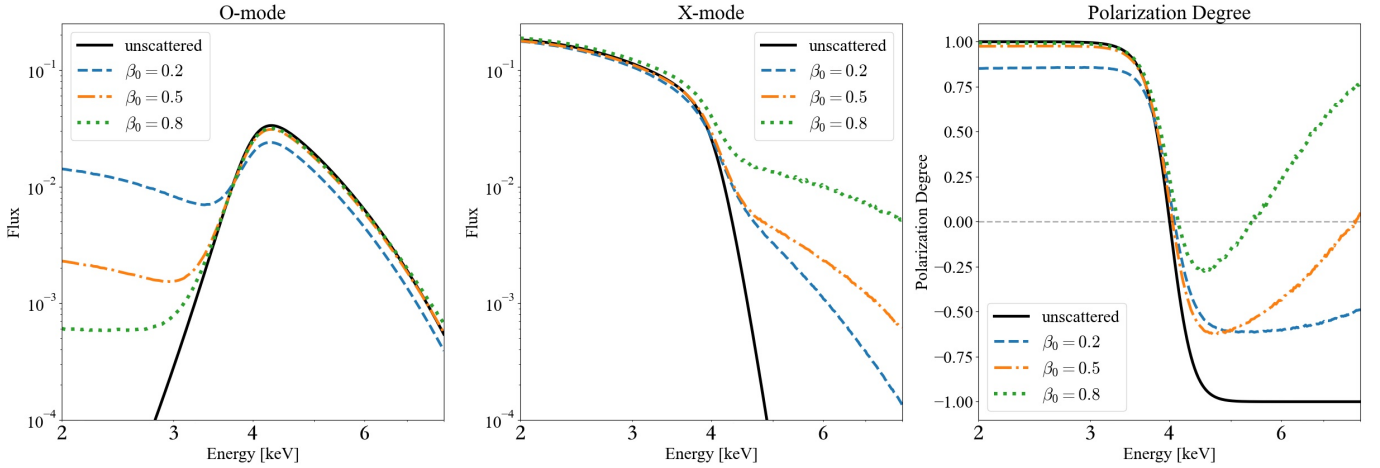


Figure 6. Flux and polarization spectra for different mean electron drift velocities in the full model. The parameters are: $B_p = 10^{14}$ G, $R = 10$ km, $kT_e = 10$ keV, $kT_s = 0.6$ keV, $\theta = 35^\circ$, $\xi_r = 0.5$, and a hot spot at $(\theta_s, \phi_s) = (53^\circ, 37^\circ)$. Results are shown for $\beta_0 = 0.2, 0.5, 0.8$, and are compared with the unscattered case.

5. SUMMARY AND DISCUSSION

We have developed a unified and analytically tractable framework to approximate how resonant Compton scattering in the magnetosphere and QED vacuum resonance in the atmosphere jointly shape the X-ray spectra and polarization observed from magnetars. Starting from the polarized radiative transfer equation (16) with scattering, we adopt a first-order approximation in optical depth (see Eqs.(17), (18) and (21)), which effectively captures single scatterings, to compute the observed polarization fluxes (Eqs.(22)-(24)). For a concrete baseline, we adopt an idealized initial surface emission polarization pattern that mimicks vacuum-resonant conversion—100% X-mode below 4 keV and 100% O-mode above, with a smooth transition in between (see D. Lai (2023))—and then quantify how RCS in the mag-

netosphere reshapes the observable polarization signatures. Our key findings are as follows:

1. Increasing the plasma density in the magnetosphere leads to an overall suppression of both the absolute value and spectral variation of polarization degree P_L . In another words, RCS acts to compress the polarization curve toward a horizontal line located *above* zero, diminishing the polarization contrast (see Figs. 2 and 5).
2. Increasing the average electron drift velocity enhances the SR effects, which tend to raise P_L in the high-energy tail and steepen its slope. In some cases, an extra mode switch (i.e., sign change in P_L , implying a 90° PA swing) induced by RCS may occur (see Figure 6).

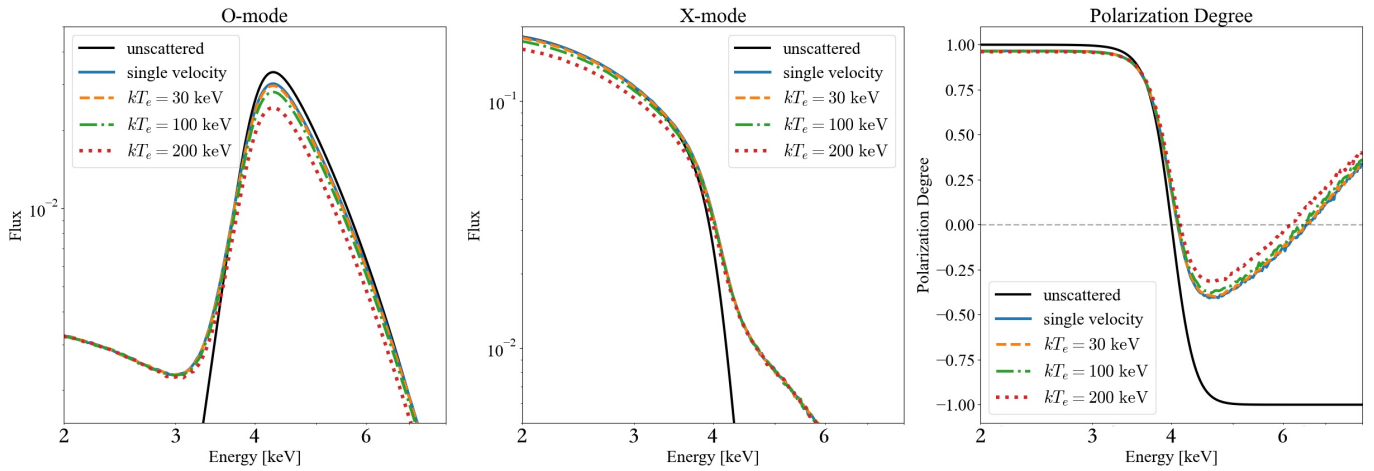


Figure 7. Flux and polarization spectra for different magnetospheric plasma temperatures in the full model. The parameters are: $B_p = 10^{14}$ G, $R = 10$ km, $kT_s = 0.6$ keV, $\theta = 35^\circ$, $\beta_0 = 0.5$, and a hot spot at $(\theta_s, \phi_s) = (53^\circ, 37^\circ)$. Results are shown for $kT_e = 30, 100, 200$ keV, and are compared with the unscattered and single-velocity cases.

3. The energy of the *first* mode switch is only weakly shifted by RCS in the parameter ranges explored here; the zero-crossing location remains largely tied to the stellar surface physics set by vacuum resonance.
4. In the strong RCS regime, the combined effects of increased plasma density and enhanced SR effects may entirely erase the signature of mode switch within the observed bandpass (2–8 keV), even when the QED-induced conversion is present in the initial emission. This is consistent with the mode-redistribution trend expected from the resonant cross sections (see Eq.(29)).

However, these conclusions should be interpreted in light of several simplifying assumptions. (i) Our magnetospheric configuration is *prescribed* rather than dynamically self-consistent. As discussed in Section 2, the field and current systems are parameterized and do not enforce full force-free equilibrium. In addition, the actual magnetosphere is likely to be partly-twisted rather than globally, and the prescribed thermal velocity distribution in magnetosphere may not capture some intrinsic physical effects (e.g., R. Fernández & C. Thompson 2007, considered a power-law distribution of relativistic momentum). (ii) Our sample results consider emission from a single surface patch. Radiation from the whole NS surface can be easily included in our formalism and will likely average out some geometric contrasts. (iii) Our transport solution is only of first order in optical depth. To fully capture the energy-dependent behavior (e.g., power-law high-energy tail and Comptonization) and energy/polarization redistribution at high RCS optical depth requires higher-order solutions via iterative scattering treatments (e.g., for 1D iterative scatterings,

see M. Lyutikov & F. P. Gavril 2006). (iv) Our adopted surface polarization pattern is idealized; a more realistic treatment would require detailed modeling of the NS surface and atmosphere.

Despite these limitations, the semi-analytic nature of our method offers a major computational advantage and physical transparency. It allows us to extract the main physical trends without the computational cost or complexity of full Monte Carlo simulations, and reveals intuitive connections between model inputs and observable outcomes.

Looking ahead, two immediate extensions are natural. First, to better capture viewing-angle-dependent effects, full-surface integration should be implemented, which would remove projection biases from small-area sources and allow more realistic modeling of observation profiles. In our formalism, this only requires treating the coordinates of the surface emission point as integration variables over solid angle. Second, including stellar rotation would allow phase-resolved predictions when the magnetic and spin axes are misaligned. In our framework, this is equivalent to a rotation of the LOS direction vector and tracking how the polarization signal evolves with phase, enabling the calculation of phase-resolved light curves and phase-averaged polarization profiles. These developments, together with higher-order scatterings, will help connect magnetar surface and magnetosphere models with observations. Upcoming X-ray polarization mission, such as eXTP (S. Zhang et al. 2016, 2019) will have greatly enhanced polarization sensitivity and extended energy band, providing simultaneous spectral, timing, and polarization data, thereby enriching the magnetar polarization sample for further studies.

REFERENCES

- Beloborodov, A. M. 2002, *Astrophys. J. Lett.*, 566, L85, doi: [10.1086/339511](https://doi.org/10.1086/339511)
- Caiazzo, I., González-Caniulef, D., Heyl, J., & Fernández, R. 2022, *MNRAS*, 514, 5024, doi: [10.1093/mnras/stac1571](https://doi.org/10.1093/mnras/stac1571)
- Duncan, R. C., & Thompson, C. 1992, *ApJL*, 392, L9, doi: [10.1086/186413](https://doi.org/10.1086/186413)
- Fernández, R., & Davis, S. W. 2011, *ApJ*, 730, 131, doi: [10.1088/0004-637X/730/2/131](https://doi.org/10.1088/0004-637X/730/2/131)
- Fernández, R., & Thompson, C. 2007, *ApJ*, 660, 615, doi: [10.1086/511810](https://doi.org/10.1086/511810)
- Heyl, J. S., Shaviv, N. J., & Lloyd, D. 2003, *Mon. Not. Roy. Astron. Soc.*, 342, 134, doi: [10.1046/j.1365-8711.2003.06521.x](https://doi.org/10.1046/j.1365-8711.2003.06521.x)
- Ho, W. C. G., & Lai, D. 2003, *MNRAS*, 338, 233, doi: [10.1046/j.1365-8711.2003.06047.x](https://doi.org/10.1046/j.1365-8711.2003.06047.x)
- Kaspi, V. M., & Beloborodov, A. M. 2017, *ARA&A*, 55, 261, doi: [10.1146/annurev-astro-081915-023329](https://doi.org/10.1146/annurev-astro-081915-023329)
- Kelly, R. M. E., Zane, S., Turolla, R., & Taverna, R. 2024, *Mon. Not. Roy. Astron. Soc.*, 528, 3927, doi: [10.1093/mnras/stae159](https://doi.org/10.1093/mnras/stae159)
- Kouveliotou, C., Dieters, S., Strohmayer, T., et al. 1998, *Nature*, 393, 235, doi: [10.1038/30410](https://doi.org/10.1038/30410)
- Lai, D. 2023, *Proceedings of the National Academy of Science*, 120, e2216534120, doi: [10.1073/pnas.2216534120](https://doi.org/10.1073/pnas.2216534120)
- Lai, D., & Ho, W. C. 2002, *ApJ*, 566, 373, doi: [10.1086/338074](https://doi.org/10.1086/338074)
- Lai, D., & Ho, W. C. 2003a, *PhRvL*, 91, 071101, doi: [10.1103/PhysRevLett.91.071101](https://doi.org/10.1103/PhysRevLett.91.071101)
- Lai, D., & Ho, W. C. 2003b, *ApJ*, 588, 962, doi: [10.1086/374334](https://doi.org/10.1086/374334)
- Lyutikov, M., & Gavriil, F. P. 2006, *MNRAS*, 368, 690, doi: [10.1111/j.1365-2966.2006.10140.x](https://doi.org/10.1111/j.1365-2966.2006.10140.x)
- Medin, Z., & Lai, D. 2006a, *PhRvA*, 74, 062507, doi: [10.1103/PhysRevA.74.062507](https://doi.org/10.1103/PhysRevA.74.062507)
- Medin, Z., & Lai, D. 2006b, *PhRvA*, 74, 062508, doi: [10.1103/PhysRevA.74.062508](https://doi.org/10.1103/PhysRevA.74.062508)
- Medin, Z., & Lai, D. 2007, *MNRAS*, 382, 1833, doi: [10.1111/j.1365-2966.2007.12492.x](https://doi.org/10.1111/j.1365-2966.2007.12492.x)
- Meszáros, P. 1992, High-energy radiation from magnetized neutron stars
- Nobili, L., Turolla, R., & Zane, S. 2008a, *MNRAS*, 386, 1527, doi: [10.1111/j.1365-2966.2008.13125.x](https://doi.org/10.1111/j.1365-2966.2008.13125.x)
- Nobili, L., Turolla, R., & Zane, S. 2008b, *MNRAS*, 389, 989, doi: [10.1111/j.1365-2966.2008.13627.x](https://doi.org/10.1111/j.1365-2966.2008.13627.x)
- Potekhin, A. Y., & Chabrier, G. 2013, *A&A*, 550, A43, doi: [10.1051/0004-6361/201220082](https://doi.org/10.1051/0004-6361/201220082)
- Rea, N., Zane, S., Turolla, R., Lyutikov, M., & Götz, D. 2008, *ApJ*, 686, 1245, doi: [10.1086/591264](https://doi.org/10.1086/591264)
- Shabaltas, N., & Lai, D. 2012, *ApJ*, 748, 148, doi: [10.1088/0004-637X/748/2/148](https://doi.org/10.1088/0004-637X/748/2/148)
- Taverna, R., Muleri, F., Turolla, R., et al. 2014, *Mon. Not. Roy. Astron. Soc.*, 438, 1686, doi: [10.1093/mnras/stt2310](https://doi.org/10.1093/mnras/stt2310)
- Taverna, R., & Turolla, R. 2024, *Galaxies*, 12, 6, doi: [10.3390/galaxies12010006](https://doi.org/10.3390/galaxies12010006)
- Taverna, R., Turolla, R., Suleimanov, V., Potekhin, A. Y., & Zane, S. 2020, *Mon. Not. Roy. Astron. Soc.*, 492, 5057, doi: [10.1093/mnras/staa204](https://doi.org/10.1093/mnras/staa204)
- Taverna, R., Turolla, R., Muleri, F., et al. 2022, *Science*, 378, 646, doi: [10.1126/science.add0080](https://doi.org/10.1126/science.add0080)
- Thompson, C., & Duncan, R. C. 1995, *MNRAS*, 275, 255, doi: [10.1093/mnras/275.2.255](https://doi.org/10.1093/mnras/275.2.255)
- Thompson, C., Lyutikov, M., & Kulkarni, S. R. 2002, *ApJ*, 574, 332, doi: [10.1086/340586](https://doi.org/10.1086/340586)
- van Adelsberg, M., & Lai, D. 2006, *Mon. Not. Roy. Astron. Soc.*, 373, 1495, doi: [10.1111/j.1365-2966.2006.11098.x](https://doi.org/10.1111/j.1365-2966.2006.11098.x)
- Ventura, J. 1979, *Phys. Rev. D*, 19, 1684, doi: [10.1103/PhysRevD.19.1684](https://doi.org/10.1103/PhysRevD.19.1684)
- Wang, C., & Lai, D. 2009, *MNRAS*, 398, 515, doi: [10.1111/j.1365-2966.2009.14895.x](https://doi.org/10.1111/j.1365-2966.2009.14895.x)
- Weisskopf, M. C., Ramsey, B., O'Dell, S., et al. 2016, in *Society of Photo-Optical Instrumentation Engineers (SPIE) Conference Series*, Vol. 9905, *Space Telescopes and Instrumentation 2016: Ultraviolet to Gamma Ray*, ed. J.-W. A. den Herder, T. Takahashi, & M. Bautz, 990517, doi: [10.1117/12.2235240](https://doi.org/10.1117/12.2235240)
- Weisskopf, M. C., Soffitta, P., Baldini, L., et al. 2022, *Journal of Astronomical Telescopes, Instruments, and Systems*, 8, 026002, doi: [10.1117/1.JATIS.8.2.026002](https://doi.org/10.1117/1.JATIS.8.2.026002)
- Woods, P. M., & Thompson, C. 2006, in *Compact stellar X-ray sources*, ed. W. H. G. Lewin & M. van der Klis, Vol. 39, 547–586, doi: [10.48550/arXiv.astro-ph/0406133](https://doi.org/10.48550/arXiv.astro-ph/0406133)
- Zane, S., Rea, N., Turolla, R., & Nobili, L. 2009, *MNRAS*, 398, 1403, doi: [10.1111/j.1365-2966.2009.15190.x](https://doi.org/10.1111/j.1365-2966.2009.15190.x)
- Zane, S., et al. 2023, *Astrophys. J. Lett.*, 944, L27, doi: [10.3847/2041-8213/acb703](https://doi.org/10.3847/2041-8213/acb703)
- Zhang, S., Feroci, M., Santangelo, A., et al. 2016, in *Society of Photo-Optical Instrumentation Engineers (SPIE) Conference Series*, Vol. 9905, *Space Telescopes and Instrumentation 2016: Ultraviolet to Gamma Ray*, ed. J.-W. A. den Herder, T. Takahashi, & M. Bautz, 99051Q, doi: [10.1117/12.2232034](https://doi.org/10.1117/12.2232034)
- Zhang, S., Santangelo, A., Feroci, M., et al. 2019, *Science China Physics, Mechanics, and Astronomy*, 62, 29502, doi: [10.1007/s11433-018-9309-2](https://doi.org/10.1007/s11433-018-9309-2)